Broadband Photodetectors Based on Graphene–Bi_2Te_3 Heterostructure

Hong Qiao,[†,∥] Jian Yuan,[†,∥] Zaiquan Xu,[‡] Caiyun Chen,[†] Shenghuang Lin,[†,§] Yusheng Wang,[†] Jingchao Song,[‡] Yan Liu,[†] Qasim Khan,[†] Hui Ying Hoh,[‡] Chun-Xu Pan,[⊥] Shaojuan Li,*[,†] and Qiaoliang Bao*[,†,‡]

[†]Institute of Functional Nano and Soft Materials (FUNSOM), Jiangsu Key Laboratory for Carbon-Based Functional Materials and Devices, and Collaborative Innovation Center of Suzhou Nano Science and Technology, Soochow University, Suzhou 215123, P. R. China, [‡]Department of Materials Engineering, Monash University, Clayton, Victoria 3800, Australia, [§]Department of Applied Physics, The Hong Kong Polytechnic University, Hung Hom, Hong Kong SAR, China, and [⊥]School of Physics and Technology, Wuhan University, Wuhan 430072, China. [∥]These authors contributed equally to this work.

ABSTRACT Recently, research on graphene based photodetectors has drawn substantial attention due to ultrafast and broadband photoresponse of graphene. However, they usually have low responsivity and low photoconductive gain induced by the gapless nature of graphene, which greatly limit their applications. The synergetic integration of graphene with other two-dimensional (2D) materials to form van der Waals heterostructure is a very promising approach to overcome these shortcomings. Here we report the growth of graphene–Bi_2Te_3 heterostructure where Bi_2Te_3 is a small bandgap material from topological insulator family with a similar hexagonal symmetry to graphene. Because of the effective photocarrier generation and transfer at the interface between graphene and Bi_2Te_3, the device photocurrent can be effectively enhanced without sacrificing the detecting spectral width. Our results show that the graphene–Bi_2Te_3 photodetector has much higher photoresponsivity (35 AW^{-1} at a wavelength of 532 nm) and higher sensitivity (photoconductive gain up to 83), as compared to the pure monolayer graphene-based devices. More interestingly, the detection wavelength range of our device is further expanded to near-infrared (980 nm) and telecommunication band (1550 nm), which is not observed on the devices based on heterostructures of graphene and transition metal dichalcogenides.

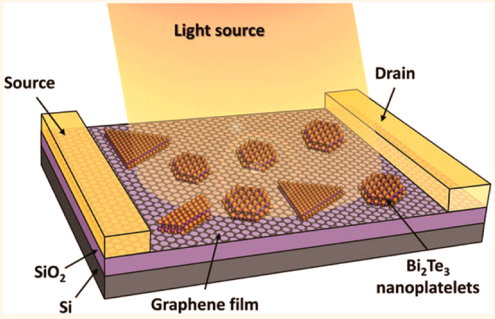

KEYWORDS: photodetector · graphene · heterostructure · broadband · photoresponsivity · sensitivity

Within the past few years, graphene, a novel two-dimensional (2D) material with a honeycomb lattice, has drawn a large amount of interest due to its extraordinary electrical and optical properties.[1] The significant wavelength-independent absorption and high carrier mobility (highest up to 200 000 $cm^2 V^{-1} S^{-1}$)[2–4] in graphene makes it a promising candidate for the new generation of photonic and optoelectronic devices, especially for light detection purposes.[5–7] The research of graphene-based photodetectors has achieved many impressive progresses because of their high response speed and broad detecting spectral width, and they show great potential to replace traditional III–V semiconductor photodetection devices. However, the gapless nature of intrinsic graphene and limited light absorption in one atomic layer ($\pi\alpha$ = 2.3%) has prevented the reported photodetectors from exhibiting efficient photocarrier separation or accumulation, which leads to the poor device performance in terms of low photoresponsivity (a few mA W^{-1}) and low photoconductive gain.[8–10]

To overcome this shortcoming, many efforts have been made. For example, band gap opening is a direct solution, which can be achieved by utilizing bilayer graphene[11,12] and graphene nanoribbons.[13] Nevertheless, such approaches have difficulties in the fabrication process, repeatability and could not guarantee better performance due to the degradation of carrier mobility in graphene.[14] On the other hand, the integration of graphene with other 2D materials with a band gap, such as transition metal dichalcogenides (TMDCs), appears to be a more promising approach. In this respect, photodetectors based on MoS_2–graphene or WSe_2–graphene heterojunction have achieved unprecedented performance in terms of high responsivity and sensitivity because of the synergistic marriage of these

* Address correspondence to sjli@suda.edu.cn, qlbao@suda.edu.cn.

Received for review November 28, 2014 and accepted January 17, 2015.

Published online January 17, 2015
10.1021/nn506920z

two 2D materials.[15−17] Furthermore, semiconducting quantum dots (QDs) can be introduced as gain material to hybridize with graphene for photodetectors, which have demonstrated ultrahigh photoconductive gain.[18]

However, the optical gap of 1−2 eV in TMDCs and PbS QDs greatly limits their application for photodetection in the near-infrared (NIR) region, especially telecommunication bands at around 1550 nm (0.8 eV).[19,20] To this point, another class of exotic 2D materials, topological insulators, mainly Bi_2Te_3, Bi_2Se_3, Sb_2Te_3, which normally have a very small band gap (0.15−0.3 eV) in the mid-infrared range, would be a better choice.[21,22]

In this paper, we present an effective broadband (from visible to infrared) photodetector based on graphene−Bi_2Te_3 heterostructure. Bi_2Te_3 crystals are typical layered materials *via* van der Waals interactions with hexagonal unit cell similar to that of graphene. The very small lattice mismatch allows large area epitaxial growth of Bi_2Te_3 nanocrystals on a graphene template,[23,24] thus forming a new van der Waals heterostructure with an atomic gapless interface, and enabling effective transfer and separation of photoexcited carriers. Another significant advantage of our heterostructure device is that the small band gap of Bi_2Te_3 allows the detection for near-infrared wavelengths and telecommunication band. Using this heterostructure material for photodetection, not only can we take advantage of the exotic properties of graphene, *i.e.*, ultrahigh carrier motilities, but we can also effectively adopt the merits of Bi_2Te_3, *i.e.*, enhanced light-matter interaction as well as reduced recombination of photoexcited carriers. In comparison with pure monolayer graphene-based devices, the graphene−Bi_2Te_3 heterostructure photodetector shows about 1000 times higher responsivity (of the order of a few tens A W^{-1}) and a high photoconductive gain (highest value around 83). Moreover, our device has comparable responsivity and gain at near-infrared (980 nm) and telecommunication wavelength (1.5 μm) with those at visible wavelength (532 nm), attesting to the capability for broadband detection.

RESULTS AND DISSCUSSION

Figure 1a shows the schematic diagram of graphene−Bi_2Te_3 heterostructure, layered Bi_2Te_3 crystals have a rhombohedral crystal structure with similar hexagonal symmetry to that of graphene, and each quintuple layer (QL) in Bi_2Te_3 is ordered in a Te−Bi−Te−Bi−Te subsequence.[25] The plan view at the right side shows the lattice matching of graphene and Bi_2Te_3 in ideal conditions. The hexagonal periodicity of Bi_2Te_3 along which the carbon atoms align in graphene is $d = 4.385$ Å, and the length of the C−C bond in graphene is ∼1.42 Å. As a result, Bi_2Te_3 has a small lattice mismatch of 2.7% (0.125 Å) with graphene, which is ideal for *van der Waals* epitaxial growth.[23,26] Practically, the van der Waals interface undergoes lattice relaxation, as usually encountered in heteroepitaxial growth of layered materials.

Bi_2Te_3 nanocrystals are epitaxially grown on monolayer graphene by chemical vapor deposition (CVD). As shown in Figure 1b, a typical scanning electron microscopy (SEM) image of the graphene−Bi_2Te_3 heterostructure, the submicrometer Bi_2Te_3 nanoplatelets were uniformly grown on the graphene substrate. The random orientation of Bi_2Te_3 nanoplatelets may result from the polycrystalline nature of the graphene film. The coverage and thickness of Bi_2Te_3 nanoplatelets can be controlled *via* tuning the concentration of seeds and growth time. Figure 1c shows a representative transmission electron microscopy (TEM) image of graphene−Bi_2Te_3 heterostructure; the hexagonal shape of the Bi_2Te_3 nanoplatelet (about 300 nm size) can be clearly seen. The high-resolution TEM (HRTEM) image (Figure 1d) shows hexagonal lattice fringes with a lattice spacing of 0.21 nm, consistent with the spacing of the $(11\bar{2}0)$ planes of layered Bi_2Te_3. The selective area electron diffraction (SAED) pattern of the corresponding area (shown in inset) exhibits a clear pattern with hexagonal symmetry, confirming the single crystalline nature of the material. It is found that the Bi_2Te_3 nanoplatelets grow along $[11\bar{2}0]$ and $[2\bar{1}\bar{1}0]$ directions, with $(01\bar{1}0)$ facets as the side surfaces and (0001) facets as the top and bottom surfaces. The thickness of the Bi_2Te_3 nanoplatelets layer is found to be around 30 nm using atomic force microscopy (AFM) (see Figure S1 in Supporting Information), which is desired for the observation of topologically conductive surface state in this type of materials.[15]

Figure 1e shows a representative Raman spectrum of the graphene−Bi_2Te_3 heterostructure excited by a 514 nm laser. The characteristic Raman peaks of both materials are clearly resolved. At the low frequency region, there are three peaks at 59, 100, and 139 cm^{-1}, which are consistent with the A_{1g}^1, E_g^2, and A_{1g}^2 vibrational modes of Bi_2Te_3 single crystals, respectively. At the high frequency region, the two characteristic peaks for graphene at 1580 cm^{-1} (G-band) and 2700 cm^{-1} (2D-band) are observed, corresponding to the stretching of the C−C bond and a second-order two-phonon process in sp^2 carbon systems, respectively. The 2D peak of the pristine graphene was well fitted by a sharp and symmetric Lorentzian peak with full-width at half-maximum (fwhm) of 23.74 cm^{-1}, which is consistent with the feature of single-layer graphene.[10,15,27] The optical absorption property of graphene−Bi_2Te_3 heterostructure was also investigated, as shown in Figure 1f. It is obvious that compared to pure graphene, the heterostructure material has enhanced light absorption over a wide range of wavelengths, which is essential for photodetection.

Figure 2a illustrates the configuration of the photodetector device based on graphene−Bi_2Te_3 heterostructure. To create a built-in electric field to effectively

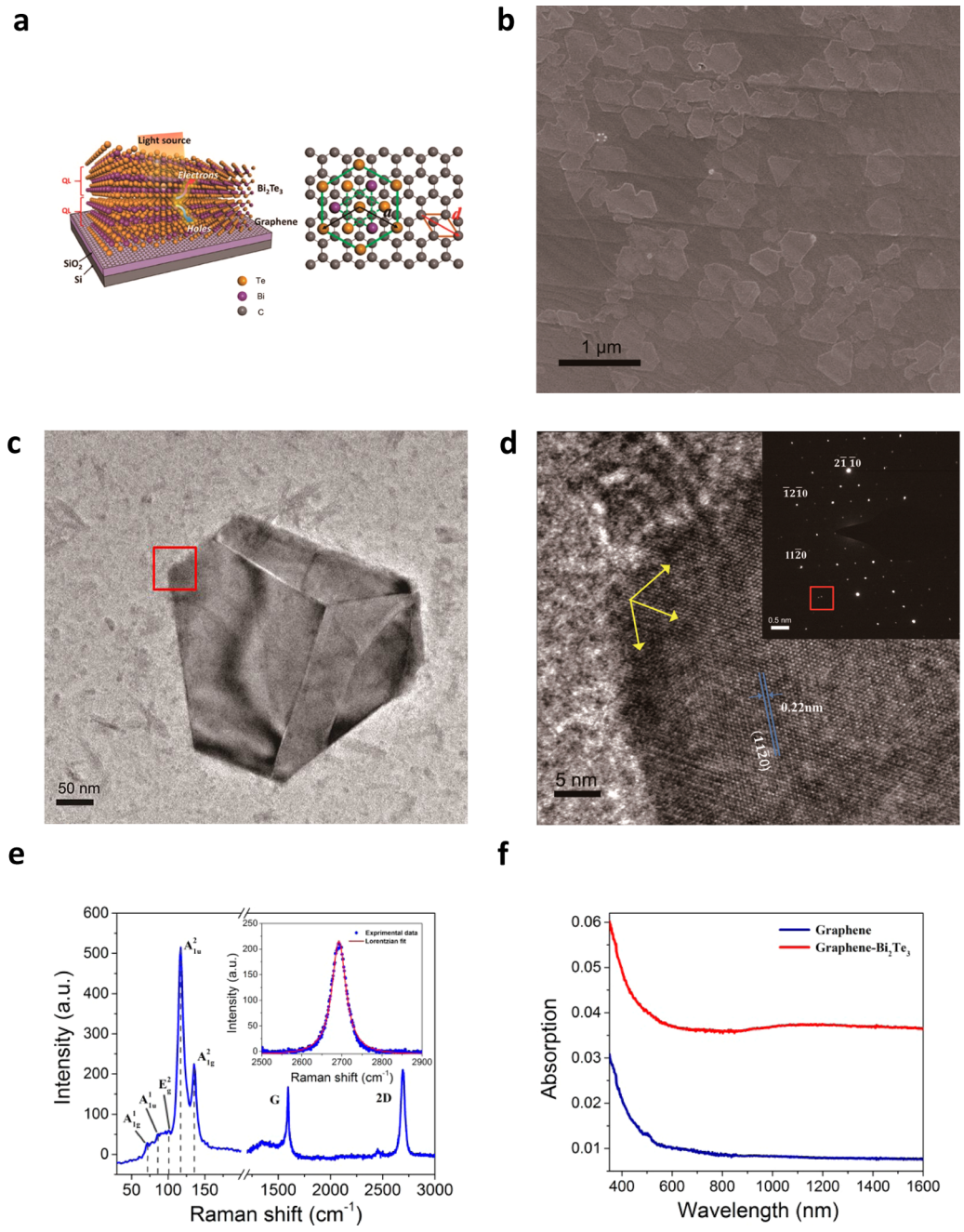

Figure 1. Material characterizations of the graphene−Bi_2Te_3 heterostructure. (a) Schematic of graphene−Bi_2Te_3 heterostructure, 3D and top view. (b) SEM image of Bi_2Te_3 nanoplatelets grown on graphene. (c) TEM image of Bi_2Te_3 nanoplatelet on graphene. (d) HRTEM image of the region marked by the red square in panel c. The yellow arrows indicate the crystal lattice orientation. Inset: SAED pattern. (e) Raman spectrum of graphene−Bi_2Te_3 heterostructure. Inset: Lorentzian fit of 2D peak of graphene. (f) UV−visible to NIR absorption spectrum of graphene and graphene−Bi_2Te_3 heterostructure.

lead out the photoexcited carriers, interdigitated electrodes with different work functions were deposited as the source and drain.[9] The detailed procedure of device fabrication is presented in the Methods section. Figure 2b shows the photocurrent results of two different devices based on monolayer graphene and graphene−Bi_2Te_3 heterostructure without applying the gate bias. The photocurrent of the graphene−Bi_2Te_3 heterostructure device is about 10 times higher than that of the pure graphene device. More importantly, the heterostructure device demonstrates broadband photoresponse from ultraviolet (UV), visible to NIR wavelength range, as shown in Figure 2c. A peak photocurrent is observed at about 580 nm, which may originate from relatively high power of the light source at this particular wavelength. It should be noted that a detectable current of about 0.5 μA can be obtained at 1550 nm, which is the telecommunication C band. We also calculated the dependence of responsivity and photoconductive gain on excitation

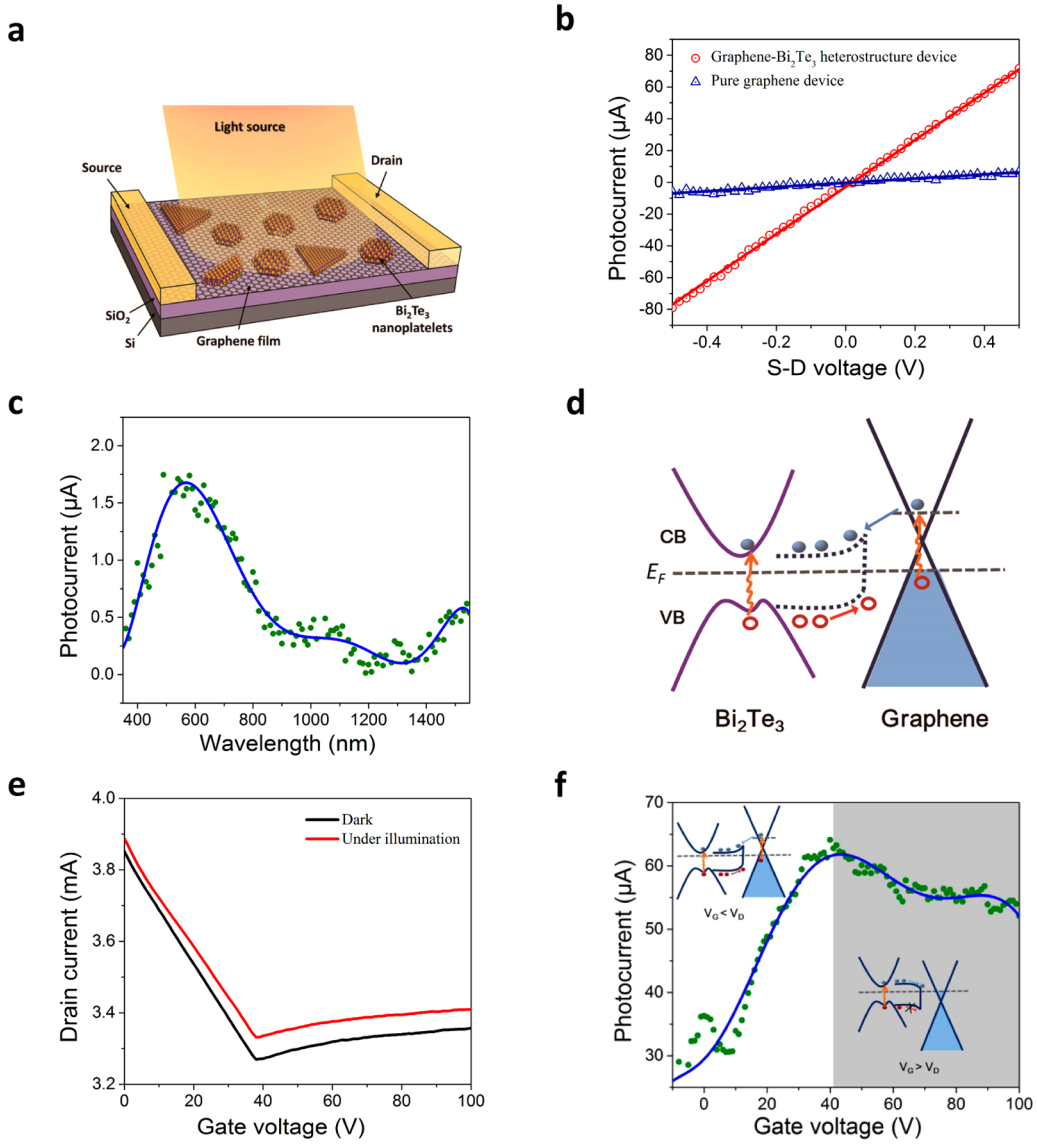

Figure 2. Device characterizations of the graphene–Bi_2Te_3 heterostructure. (a) Schematic of the heterostructure phototransistor device. (b) Dependence of photocurrent on source-drain voltage. The circles and triangles are experimental data, while the red and blue lines are linear fit curves. (c) Photocurrent of the heterostructure device as a function of photoexcitation wavelength (from 400 to 1550 nm). The green dots are experimental data, and the blue line is a guide to eyes. (d) Energy band diagram of graphene–Bi_2Te_3 heterojunction. The blue dots stand for the photogenerated electrons, while red hollow dots stand for holes. (e) Drain current as a function of gate voltage with and without illumination. Source-drain bias $V_{S\text{-}D} = 0.2$ V, excitation wavelength $\lambda = 532$ nm. (f) Photocurrent as a function of gate voltage. This curve is calculated from panel e. Inset: Energy diagrams of the heterostructure where $V_G < V_D$ and $V_G > V_D$.

wavelength and the results are shown in Figure S6 in Supporting Information. The optical response measurements at specific wavelengths will be discussed later.

To explain the highly enhanced photocurrent in our new photodetector device, an energy diagram is proposed to elucidate the transfer of photoexcited carriers in graphene–Bi_2Te_3 heterostructure, as shown in Figure 2d. It is well-known that the Fermi level of as-grown graphene samples are located below the Dirac point because of the doping effect of substrates, defects, water molecules and oxygen in air.[28] In contrast, the as-grown Bi_2Te_3 nanocrystals have an n-type bulk state due to Te vacancies,[29,30] and its Fermi level locates above the bottom of bulk conduction band.[31] As a result, a Schottky-like junction forms at the interface of graphene and Bi_2Te_3 as the electrons from Bi_2Te_3 will be injected into graphene. Thus, the direction of band bending arises from Bi_2Te_3 to graphene, similar to a semiconductor–metal contact. Driven by the built-in electrical field, photoexcited electrons in graphene can move into the conduction band of Bi_2Te_3 upon light illumination, while photogenerated holes remain at the valence band of graphene. On the other hand, Bi_2Te_3 can also absorb light and create electron–hole pairs. Electrons will be trapped inside Bi_2Te_3

because of the energy barrier, while holes can be injected to the valence band of graphene. Consequently, recombination of photogenerated carriers can be suppressed effectively and the number of majority carriers (holes) in graphene can be increased, which in turn gives rise to a larger photocurrent in the device based on these heterostructure.

To further characterize graphene−Bi_2Te_3 heterostructure device, we investigate the gate dependent photoelectrical performance, as shown in Figure 2e. The minimum drain current occurs when the gate voltage is 37 V, corresponding to the charge neutral point (similar to Dirac point in graphene, *i.e.*, $V_D = 37$ V). This suggests that the graphene−Bi_2Te_3 heterostructure is still p-type doped even though the carrier injection from Bi_2Te_3 is supposed to weaken the doping effect in graphene caused by the silicon substrate. Enhancement of light-induced drain current is clearly observed when certain back gate bias is applied (Figure 2e) and the corresponding photocurrent as a function of gate voltage V_G is depicted in Figure 2f. The carrier transport is hole-dominated for $V_G < V_D$ and electron-doped for $V_G > V_D$. The photocurrent rises with increasing gate voltage when $V_G < V_D$ and a peak is observed at the charge neutral point, then the photocurrent slightly declines when gate voltage increases ($V_G > V_D$). This can be well explained by the energy diagram (Figure 2f). For $V_G < V_D$, graphene is hole-doped; increase of gate voltage shifts the Fermi energy in graphene to a higher level which facilitates the injection of more holes from Bi_2Te_3 to graphene, resulting in the enhancement of photocurrent until it reaches the maximum value at the charge neutral point. For $V_G > V_D$, the Fermi level of graphene is shifted to above the Dirac point, and the majority carriers change from holes to electrons which does not change the polarity of photocurrent. In this case, the injection of photoexcited electrons from Bi_2Te_3 to graphene becomes the dominating mechanism of photocurrent generation. As the increasing gate voltage continues to shift the Fermi level in graphene upward, the built-in electric field caused by the heterojunction becomes smaller, so fewer electrons can be transferred to graphene, leading to a slight decrease in the photocurrent. In addition, it is noted that the rate of decrease in photocurrent in the n-type region is lower than the rate of increase in the p-type region; this may be attributed to the difference in the rate of change of photoconductivity in these two regions. The rate of change in photoconductivity $\Delta\sigma_n$ for n-type region and $\Delta\sigma_p$ for p-type region can be formulated by $\Delta\sigma_n = q \cdot \Delta n \cdot \mu_n$ and $\Delta\sigma_p = q \cdot \Delta p \cdot \mu_p$, where q is the charge for electrons, Δn and Δp are the carrier concentration of electrons and holes, respectively, and μ_n and μ_p represent the electron and hole mobility, respectively. As indicated by the transfer curve of Figure 2e, the electron mobility μ_n is lower than the hole mobility μ_p; consequently, we can get $\Delta\sigma_n < \Delta\sigma_p$ (considering that Δn and Δp are the same).

With the aim to demonstrate the capability of broadband detection and high sensitivity of our device, a series of photoelectric measurements were performed at different specific wavelengths. First, we study the device response under illumination of a visible light source (532 nm). Figure 3a shows the device response to pulsed light at an optical pumping of 115 μW. The photocurrent of the graphene−Bi_2Te_3 heterostructure device can be effectively switched on and off while the light source is turned on and off. A steady photocurrent of about 170 μA can be measured at the on state. A rising time of about 8.7 ms (see Figure S3 in Supporting Information) suggests a relatively fast photoresponse. The illumination power dependence is also studied and the results are shown in Figure 3b. The photocurrent increases nonlinearly as the incident power is turned up from 6 μW, while the corresponding photoresponsivity decreases exponentially with increasing power. Increase in the photoexcited carrier concentration caused by higher incident power produces an electrical field opposite to the built-in field at the junction between graphene and Bi_2Te_3, which will hamper the separation and transport of photogenerated electron−hole pairs. On the other hand, unoccupied states in the valence band of graphene decreases as the power intensity increases.[18] Moreover, this effect may also be related to the trap states in graphene or between graphene and the SiO_2 substrate, similar to the situation of single layer MoS_2 phototransistor.[32]

We further measured the optical response of the heterostructure device under illumination of NIR light at 980 and 1550 nm. Figure 3c shows photocurrent curves dependent on source-drain bias which was measured under illumination of 980 nm light at different incident powers. The photoresponse is also investigated at the telecommunication band of 1550 nm, as shown in Figure 3d. The photocurrent can be effectively turned on and off, and can be modulated by different light powers, similar to the case measured under visible light. To further investigate the device performance at different excitation wavelength, we calculated the photoresponsivity and photoconductive gain at visible and NIR illumination respectively and put them in comparison, as shown in Figure 3e,f. From Figure 3e, we can find that the highest photoresponsivity at visible region (532 nm) is determined to be about 35 A W^{-1} at an excitation power of 1.28 μW, which is, by magnitude, 1000 times larger than that of devices based on pure monolayer graphene.[8,9,33] The responsivity obtained under NIR light (980 nm) is also large enough (*i.e.*, almost 10 A W^{-1}). However, the responsivity measured at telecommunication band (1550 nm) is relative low, probably caused by the low excited photon energy. To further understand the photosensitivity of our heterostructure photodetector,

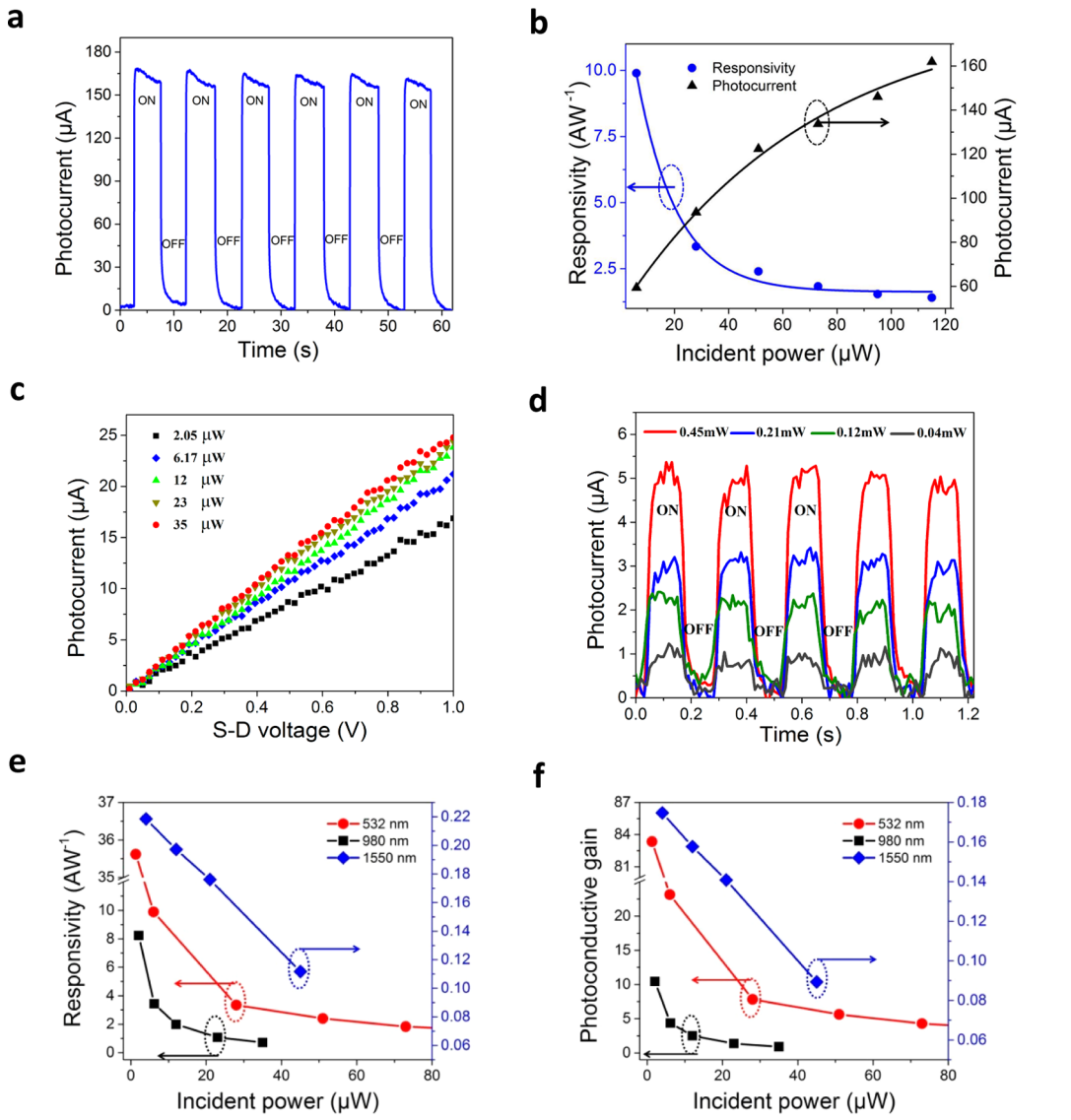

Figure 3. Photoelectric measurements under visible and NIR light illumination. (a) Time-dependent photocurrent excited by pulsed light at 532 nm. The excitation power is 115 μW, source-drain bias $V_{S\text{-}D}$ = 1 V. (b) Dependence of photocurrent and photoresponsivity on incident light power (at 532 nm). The black and blue dots are original data; the blue line is exponential fit, while black line is just a guide to eyes. (c) Photocurrent as a function of source-drain bias under the illumination of 980 nm laser with different power. (d) Time-dependent photocurrent excited by pulsed light at 1550 nm with different incident power. (e) Device photoresponsivity as a function of incident power at 532, 980, and 1550 nm, respectively. (f) Device photoconductive gain as a function of incident power at 532, 980, and 1550 nm, respectively.

we calculate the photoconductive gain of the device. The definition of photoconductive gain of a photoconductive device is the numbers of photoexcited carriers generated by per absorbed photons and per unit time, and can be expressed as $G = (I_{ph}/e\varphi(\lambda)) = ((I_{ph} \times hv)/(P(\lambda)e)) = R \times (hc/\lambda e)$.[34−36] The photoconductive gain is linearly correlated with the photoresponsivity, and the corresponding results are shown in Figure 3f. It is found that the dependence of photoconductive gain on incident power is similar to that of responsivity at each specific wavelength. The highest photoconductive gain is calculated to be 83 with the excitation of 532 nm light, indicating as many as 83 photoexcited carriers generated by per absorbed photon.

To identify the role of Bi_2Te_3 in photocurrent generation, we performed Raman and photocurrent mapping measurements on graphene−Bi_2Te_3 heterostructure device, as shown in Figure 4. The optical image of heterostructure device with interdigital electrodes is shown in Figure 4a. Figure 4b shows the Raman image integrated with the characteristic peaks of Bi_2Te_3 (from 50 to 250 cm^{-1}) and Figure 4c shows the Raman image integrated with the Si peak at 521 cm^{-1}. It is clearly seen that the regions with the strongest Si signal (outlined by dashed black lines in Figure 4c) correspond to the regions with lowest Bi_2Te_3 signal (outlined by dashed black lines in Figure 4b). This is because Bi_2Te_3 nanoflakes are not uniformly

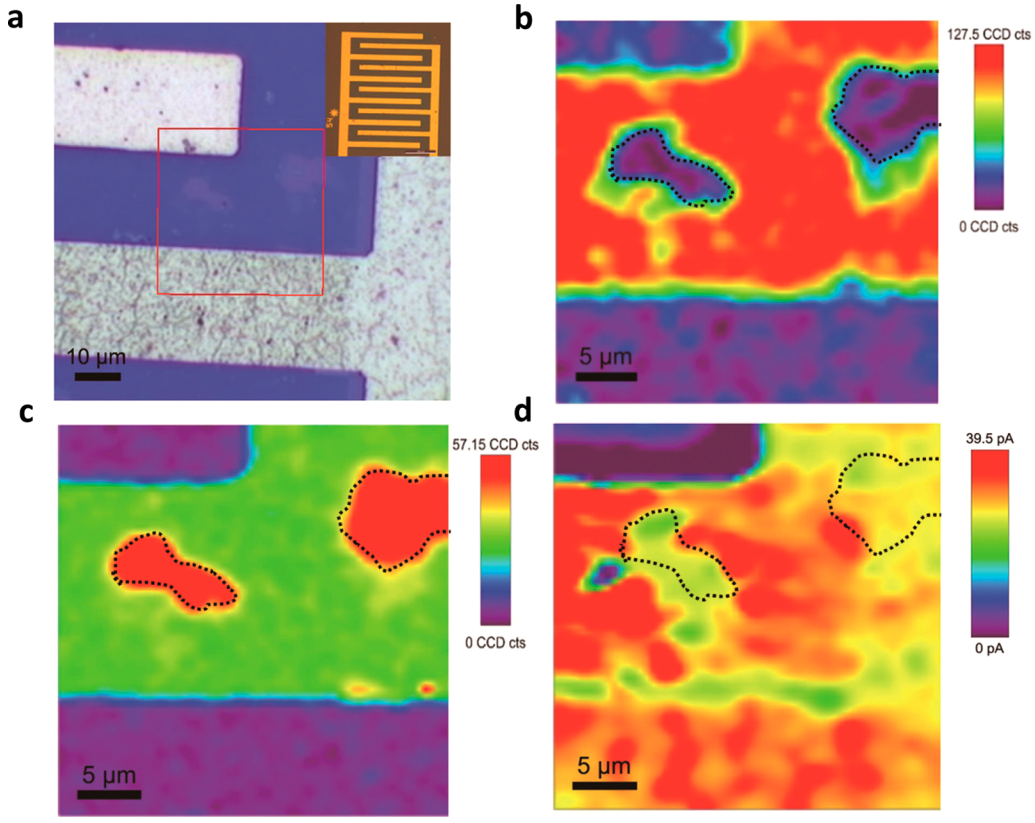

Figure 4. Raman and photocurrent image of graphene−Bi_2Te_3 heterostructure device. (a) Optical image of the measured device; the area inside the red box is the scanned area. Inset: Optical image at a lower magnification. (b) Raman map by integrating the peaks from 50 to 250 cm^{-1} of Bi_2Te_3. (c) Raman map by integrating Si peak at 521 cm^{-1}. (d) Scanning photocurrent mapping results of the graphene−Bi_2Te_3 heterostructure device. The amplitude of the measured photocurrent is represented by different colors as depicted by the scale bar.

distributed during the growth. Figure 4d shows the distribution of the photocurrent over the whole scanning area. By correlating the local materials distribution with the photocurrent mapping image, it is found that the photocurrent is significantly higher in Bi_2Te_3-rich areas (red region in Figure 4b). In contrast, the photocurrent is reasonably low in areas without Bi_2Te_3 (red region in Figure 4c). It is interesting to see that part of the interface between these two phases exhibits enhanced photocurrent generation (red region along the dashed black lines in Figure 4d). On the basis of these observations, it is concluded that Bi_2Te_3 nanoplatelets play an important role for the photocurrent enhancement in the graphene−Bi_2Te_3 heterostructure device.

CONCLUSION

In summary, we have demonstrated a highly effective photodetector based on graphene−Bi_2Te_3 heterostructure system. By combining the unique properties of graphene and Bi_2Te_3, the device not only shows greatly enhanced responsivity (of the order of a few tens A W^{-1}) and an ultrahigh photoconductive gain (up to 83), but also has the capability for broadband photodetection from visible to NIR wavelengths. This work proves that efficient electronic coupling of graphene with another small band gap 2D material will achieve superior performance compared to pure graphene based devices, thus opening new pathways for other optoelectronic functionalities or energy-harvesting applications.

METHODS

Synthesis and Characterization of Graphene−Bi_2Te_3 Heterostructure Material. Graphene films were grown on 25 μm thick copper foils (Alfa Aesar, item no. 13382) in a typical CVD system.[27] Bi_2Te_3 nanoplatelets were produced by physical vapor deposition method in a separate tube furnace. Bi_2Te_3 powder (Alfa Aesar, purity: 99.999%) was placed in the center of the furnace (about 500 °C) as the source material for evaporation. The graphene/SiO_2 substrates were then placed in the region with a temperature range of 290−360 °C. Argon was used as the carrier gas to transport the Bi_2Te_3 vapor onto the graphene films.

The morphology of the graphene−Bi_2Te_3 heterostructure was investigated in SEM (FEI Quanta 200 FEG, acceleration voltage: 5−30 kV) and the microstructure was investigated in TEM (FEI Tecnai F30, acceleration voltage: 200 kV).

Fabrication of Graphene−Bi_2Te_3 Heterostructure Devices. The photodetector devices were fabricated on highly doped n-type

silicon wafer with 300 nm oxidization layer. A typical device fabrication process includes UV lithography to define the device pattern, and electron-beam evaporation to deposit titanium and gold electrodes. The electrodes are asymmetric, the source is Au (100 nm) and the drain is Ti/Au (50 nm/50 nm). To avoid the damage to Bi_2Te_3 nanoplatelets and reduce contaminations during the fabrication process, Bi_2Te_3 nanoplatelets were epitaxially grown on intrinsic graphene after device fabrication.

Optoelectronic Measurements. Photoelectric measurements at visible wavelength range was performed at room temperature in ambient conditions using a probe station (Cascade M150) equipped with a semiconductor property analyzer (Keithley 2400). Photoelectric measurements at NIR region were carried out on an optical microscopy platform (Nea Spec) which could couple and focus IR light onto a desired location of the sample. The devices were wire-bonded prior to electrical measurements, and a double channel source-meter (Keithley 2614B) was used to collect the electrical signals. The Raman spectrum and photocurrent mapping measurements were conducted on a microconfocal-Raman system (WITec alpha 300R) which is described in Supporting Information.

Conflict of Interest: The authors declare no competing financial interest.

Acknowledgment. We acknowledge the support from the National High Technology Research and Development Program of China (863 Program) (Grant No. 2013AA031903), the youth 973 program (2015CB932700), the National Natural Science Foundation of China (Grant No. 51222208, 51290273, 91433107), the Doctoral Fund of Ministry of Education of China (Grant No. 20123201120026), ARC DECRA (DE120101569), DP (DP140101501) and Engineering Seed Funding Scheme (2014) in Monash University. This work was performed in part at the Melbourne Centre for Nanofabrication (MCN) in the Victorian Node of the Australian National Fabrication Facility (ANFF). S. Li acknowledges the support from the Natural Science Foundation of Jiangsu Province (No. BK20130328), China Postdoctoral Science Foundation (No. 2014M551654) and Jiangsu Province Postdoctoral Science Foundation (No. 1301020A).

Supporting Information Available: Details of the surface topography characterization of graphene−Bi_2Te_3 heterostructure, device electrical properties and supplementary photoelectrical results at NIR excitation, photoconductive gain calculation and scanning photocurrent mapping microscopy technique. This material is available free of charge *via* the Internet at http://pubs.acs.org.

REFERENCES AND NOTES

1. Geim, A. K.; Novoselov, K. S. The Rise of Graphene. *Nat. Mater.* **2007**, *6*, 183–191.
2. Bolotin, K. I.; Sikes, K.; Jiang, Z.; Klima, M.; Fudenberg, G.; Hone, J.; Kim, P.; Stormer, H. Ultrahigh Electron Mobility in Suspended Graphene. *Solid State Commun.* **2008**, *146*, 351–355.
3. Morozov, S.; Novoselov, K.; Katsnelson, M.; Schedin, F.; Elias, D.; Jaszczak, J.; Geim, A. Giant Intrinsic Carrier Mobilities in Graphene and Its Bilayer. *Phys. Rev. Lett.* **2008**, *100*, 016602.
4. Schedin, F.; Geim, A.; Morozov, S.; Hill, E.; Blake, P.; Katsnelson, M.; Novoselov, K. Detection of Individual Gas Molecules Adsorbed on Graphene. *Nat. Mater.* **2007**, *6*, 652–655.
5. Falkovsky, L. A. Optical Properties of Graphene And IV-VI Semiconductors. *Phys.-Usp.* **2008**, *51*, 887.
6. Novoselov, K.; Geim, A. K.; Morozov, S.; Jiang, D.; Katsnelson, M.; Grigorieva, I.; Dubonos, S.; Firsov, A. Two-Dimensional Gas of Massless Dirac Fermions in Graphene. *Nature* **2005**, *438*, 197–200.
7. Cho, S.; Fuhrer, M. S. Charge Transport and Inhomogeneity Near the Minimum Conductivity Point in Graphene. *Phys. Rev. B* **2008**, *77*, 081402.
8. Xia, F.; Mueller, T.; Lin, Y.-M.; Valdes-Garcia, A.; Avouris, P. Ultrafast Graphene Photodetector. *Nanotechnology* **2009**, *4*, 839–843.
9. Mueller, T.; Xia, F.; Avouris, P. Graphene Photodetectors for High-speed Optical Communications. *Nat. Photonics* **2010**, *4*, 297–301.
10. Zhang, Y.; Liu, T.; Meng, B.; Li, X.; Liang, G.; Hu, X.; Wang, Q. J. Broadband High Photoresponse from Pure Monolayer Graphene Photodetector. *Nat.Commun.* **2013**, *4*, 1811.
11. Fekete, L.; Hlinka, J.; Kadlec, F.; Kuzel, P.; Mounaix, P. Active Optical Control of the Terahertz Reflectivity of High-Resistivity Semiconductors. *Opt. Lett.* **2005**, *30*, 1992–1994.
12. Fekete, L.; Kadlec, F.; Nemec, H.; Kužel, P. Fast One-Dimensional Photonic Crystal Modulators for the Terahertz Range. *Opt. Exp.* **2007**, *15*, 8898–8912.
13. Chen, H.-T.; Padilla, W. J.; Zide, J. M.; Gossard, A. C.; Taylor, A. J.; Averitt, R. D. Active Terahertz Metamaterial Devices. *Nature* **2006**, *444*, 597–600.
14. Bao, Q.; Loh, K. P. Graphene Photonics, Plasmonics, and Broadband Optoelectronic Devices. *ACS Nano* **2012**, *6*, 3677–3694.
15. Roy, K.; Padmanabhan, M.; Goswami, S.; Sai, T. P.; Ramalingam, G.; Raghavan, S.; Ghosh, A. Graphene-MoS_2 Hybrid Structures for Multifunctional Photoresponsive Memory Devices. *Nat. Nanotechnol.* **2013**, *8*, 826–830.
16. Yu, W. J.; Liu, Y.; Zhou, H.; Yin, A.; Li, Z.; Huang, Y.; Duan, X. Highly Efficient Gate-tunable Photocurrent Generation in Vertical Heterostructures of Layered Materials. *Nat. Nanotechnol.* **2013**, *8*, 952–958.
17. Zhang, W.; Chuu, C.-P.; Huang, J.-K.; Chen, C.-H.; Tsai, M.-L.; Chang, Y.-H.; Liang, C.-T.; Chen, Y.-Z.; Chueh, Y.-L.; He, J.-H.; Chou, M.-Y.; Li, L.-J. Ultrahigh-Gain Photodetectors Based on Atomically Thin Graphene-MoS_2 Heterostructures. *Sci. Rep.* **2014**, 4.
18. Konstantatos, G.; Badioli, M.; Gaudreau, L.; Osmond, J.; Bernechea, M.; de Arquer, F. P. G.; Gatti, F.; Koppens, F. H. Hybrid Graphene-Quantum Dot Phototransistors with Ultrahigh Gain. *Nat. Nanotechnol.* **2013**, *7*, 363–368.
19. Kumar, A.; Ahluwalia, P. Electronic Structure of Transition Metal Dichalcogenides Monolayers 1H-MX2 (M= Mo, W; X= S, Se, Te) from *ab Initio* Theory: New Direct Band Gap Semiconductors. *Eur. Phys. J. B* **2012**, *85*, 1–7.
20. Mak, K. F.; Lee, C.; Hone, J.; Shan, J.; Heinz, T. F. Atomically Thin MoS_2: A New Direct-Gap Semiconductor. *Phys. Rev. Lett.* **2010**, *105*, 136805.
21. Fa-Xian, X.; Tong-Tong, Z. Topological Insulator Nanostructures And Devices. *Chin. Phys. B* **2013**, *22*, 96104–96117.
22. Hasan, M. Z.; Kane, C. L. Colloquium: Topological Insulators. *Rev. Mod. Phys.* **2010**, *82*, 3045.
23. Dang, W.; Peng, H.; Li, H.; Wang, P.; Liu, Z. Epitaxial Heterostructures of Ultrathin Topological Insulator Nanoplate and Graphene. *Nano Lett.* **2010**, *10*, 2870–2876.
24. Gao, G.; Gao, W.; Cannuccia, E.; Taha-Tijerina, J.; Balicas, L.; Mathkar, A.; Narayanan, T.; Liu, Z.; Gupta, B. K.; Peng, J. Artificially Stacked Atomic Layers: Toward New van der Waals Solids. *Nano Lett.* **2012**, *12*, 3518–3525.
25. Kong, D.; Dang, W.; Cha, J. J.; Li, H.; Meister, S.; Peng, H.; Liu, Z.; Cui, Y. Few-Layer Nanoplates of Bi_2Se_3 and Bi_2Te_3 with Highly Tunable Chemical Potential. *Nano Lett.* **2010**, *10*, 2245–2250.
26. Utama, M. I. B.; Belarre, F. J.; Magen, C.; Peng, B.; Arbiol, J.; Xiong, Q. Incommensurate van der Waals Epitaxy of Nanowire Arrays: A Case Study with ZnO on Muscovite Mica Substrates. *Nano Lett.* **2012**, *12*, 2146–2152.
27. Li, X.; Cai, W.; An, J.; Kim, S.; Nah, J.; Yang, D.; Piner, R.; Velamakanni, A.; Jung, I.; Tutuc, E. Large-Area Synthesis of High-Quality and Uniform Graphene Films on Copper Foils. *Science* **2009**, *324*, 1312–1314.
28. Shi, Y.; Fang, W.; Zhang, K.; Zhang, W.; Li, L. J. Photoelectrical Response in Single-Layer Graphene Transistors. *Small* **2009**, *5*, 2005–2011.
29. Xia, Y.; Qian, D.; Hsieh, D.; Wray, L.; Pal, A.; Lin, H.; Bansil, A.; Grauer, D.; Hor, Y.; Cava, R. Observation of a Large-Gap Topological-Insulator Class with a Single Dirac Cone on the Surface. *Nat, Phys.* **2009**, *5*, 398–402.
30. Bos, J.; Zandbergen, H.; Lee, M.-H.; Ong, N.; Cava, R. Structures and Thermoelectric Properties of the Infinitely

Adaptive Series $(Bi_2)_m(Bi_2Te_3)_n$. *Phys. Rev. B* **2007**, *75*, 195203.
31. Chen, Y.; Analytis, J.; Chu, J.-H.; Liu, Z.; Mo, S.-K.; Qi, X.-L.; Zhang, H.; Lu, D.; Dai, X.; Fang, Z. Experimental Realization of a Three-Dimensional Topological Insulator, Bi_2Te_3. *Science* **2009**, *325*, 178–181.
32. Lopez-Sanchez, O.; Lembke, D.; Kayci, M.; Radenovic, A.; Kis, A. Ultrasensitive Photodetectors Based on Monolayer MoS_2. *Nat. Nanotechnol.* **2013**, *8*, 497–501.
33. Lemme, M. C.; Koppens, F. H.; Falk, A. L.; Rudner, M. S.; Park, H.; Levitov, L. S.; Marcus, C. M. Gate-Activated Photoresponse in a Graphene p−n Junction. *Nano Lett.* **2011**, *11*, 4134–4137.
34. Hu, L.; Yan, J.; Liao, M.; Wu, L.; Fang, X. Ultrahigh External Quantum Efficiency from Thin SnO_2 Nanowire Ultraviolet Photodetectors. *Small* **2011**, *7*, 1012–1017.
35. Wu, P.; Dai, Y.; Sun, T.; Ye, Y.; Meng, H.; Fang, X.; Yu, B.; Dai, L. Impurity-Dependent Photoresponse Properties in Single CdSe Nanobelt Photodetectors. *ACS Appl. Mater. Interfaces* **2011**, *3*, 1859–1864.
36. Wu, P.; Dai, Y.; Ye, Y.; Yin, Y.; Dai, L. Fast-Speed and High-Gain Photodetectors of Individual Single Crystalline Zn_3P_2 Nanowires. *J. Mater. Chem.* **2011**, *21*, 2563–2567.